Running head: INTERNAL STRUCTURE OF MASSIVE DIVISION IN EXPERIMENTAL GRAVITY FLOW DEPOSITS

VISUALIZATION OF THE INTERNAL STRUCTURE OF THE MASSIVE DIVISION IN EXPERIMENTAL SEDIMENT-GRAVITY-FLOW DEPOSITS BY MAPPING OF GRAIN-FABRIC

HAJIME NARUSE and FUJIO MASUDA

Department of Geology and Mineralogy, Graduate School of Science, Kyoto University, Kitashirakawa-oiwakecho, Sakyo-ku, Kyoto 606-8224, Japan.

e-mail: naruse@kueps.kyoto-u.ac.jp

Keywords: Debris-flow deposit, grain-fabric, image analysis, massive, sediment gravity flow

Abstract: A method for mapping of grain-fabric is proposed for analysis of the cryptic internal structure of massive sedimentary units. The method is applied to the analysis of an experimental debris-flow deposit, revealing a number of characteristic features of this type of mass sedimentation. The debris-flow was simulated in the laboratory using a channel inclined 30° opening onto a 10° slope, and transverse thin sections were prepared from four longitudinal points in the depositional lobe. Back-scattered electron images of the sections obtained by scanning electron microscopy were processed and analyzed by mapping of grain-fabric using an automated image-analysis procedure. Although the samples appear structureless by macroscopic observation, the grain-fabric map reveals a range of sedimentary features, including distinctive lineations from lower-upcurrent to upper-downcurrent in the most proximal section representing synsedimentary thrusts, a steepening-upward trend of grain imbrication angle in intermediate samples with very low-angle imbrication in the basal horizon, indicative of high-shear-rate flow, and complex imbrication features in the most distal samples. This analysis reveals that massive debris-flow deposits actually contain a range of distinctive structures which are characteristic of the mode of deposition and which are not identifiable by visible inspection or analysis of grain size or color. The proposed method is therefore of great utility for the investigation and characterization of massive deposits.

INTRODUCTION

Massive sedimentary structures are macroscopically featureless units that commonly occur in sandy deposits associated with high-density sediment gravity flows, which represent a major sediment transport process in the deep-sea environment. However, despite the common occurrence of massive sandy units (Stow

and Johansson 2000), there remains some controversy as to the sedimentary processes that result in their formation. Massive structures were first identified as a feature of turbidites by Bouma (1962), who recognized the massive unit as a characteristic repeating division (Ta) in the 'Bouma sequence', the best-known turbidite facies model. Lowe (1982) interpreted the massive structure as a product of rapid deposition from a high-density turbidity current, assigning the massive unit as the S3 division of the 'Lowe Sequence'. However, debris-flows are also known to produce massive deposits, and Shanmugam (1996) suggested that massive sandy deposits should be interpreted not as deposits of high-density turbidity currents but as deposits of sandy debris-flows. This controversy has proved difficult to reconcile (e.g., Slatt et al. 1997) due to an inability to reproduce the depositional processes leading to the formation of massive structures. Although rapid deposition (Lowe 1988; Arnott and Hand 1989; Allen 1991) and "freezing" deposition of debris-flows (Postma 1986; Shanmugam 2000) have been proposed as processes forming massive structures, the true depositional mechanism is impossible to determine by conventional observations because massive structures by definition do not exhibit characteristic features and thus appear similar regardless of the depositional process (Sohn 1997).

The macroscopically featureless nature of massive structures is, of course, the reason why such structures are so difficult to analyze. Sedimentary structures are usually visible at the macroscopic level because of differences in grain size and type. For example, traction processes result in laminae due to grains sorting in size and density, and the grain-size contrast between laminae allow individual laminae to be differentiated, providing clues for the interpretation of paleo-flow conditions. In contrast, massive structures are formed by depositional processes that do not impart any grain sorting, and as such do not produce visible sedimentary features that may

aid interpretation. Therefore, to find traces of such “invisible” processes, depositional properties other than grain size should be examined.

To this end, a new visualization method is presented in this study. The technique, called grain-fabric mapping, elucidates the “invisible” sedimentary structure by measuring local oscillations of the grain-fabric rather than grain size or color. Grain-fabric is defined here as the tendency of orientation of grain elongation axes, and is known to be useful for estimation of the paleocurrent direction (Taira and Scholle 1979). The method is implemented by automated digital image analysis of thin sections for grain-fabric measurement. Although manual thin-section analysis has long been used for grain-fabric measurement (e.g., Yaghishita 1994), the manual measurement of numerous grains over a large area is difficult and time consuming. The anisotropy of magnetic susceptibility, which has also been measured in manual grain-fabric analysis (Taira 1989), is also of little use for analysis of local oscillations of grain-fabric in a single sample. Automated analysis has been made possible by recent progress in image analysis, allowing numerous grains to be analyzed over a large area (e.g., van den Berg et al. 2003). The automated grain-fabric analysis method is applied in the present study to deposits produced under controlled depositional conditions to allow comparison of fabric features with known depositional processes.

The present paper analyses an experimental flow that contain no significant cohesive mud fraction. The mud-free deposit was chosen as a first example of the grain fabric mapping method because examination of muddy deposits is relatively difficult for the automated image analysis. Herein, the term 'debris flow' is used to denote simply a high-concentration sediment flow in a laminar state. The experimental flow would be termed a hyperconcentrated density flow in the

classification scheme of Mulder and Alexander (2001), or a granular flow in the terminology of Iverson (1997). Estimates of key dimensionless ratios are presented in a later section that rigorously defines flow type (c.f. Iverson, 1997). Of course, the role of the cohesive mud fraction in natural debris flows may be important. Deposits of muddy flows will be examined in future studies.

EXPERIMENTAL DEBRIS-FLOW DEPOSITION

Debris-flow deposits were produced experimentally from a laminar-state sediment gravity flow in a channel 2 m in length, 0.25 m in width, and 0.35 m in depth (Fig. 1). The channel slope was 30°, with the mouth opening onto a slope of 10° over an area 1.8 m long by 0.9 m wide. The channel was fitted with a gate to control the release of sediment. The sediment was added to tap water upcurrent of the gate. The sediment (50 vol%) was artificial sand with a small amount of natural beach sand consisting mainly of quartz particles (mean grain size, 3.3phi; standard deviation, 1.4phi). The sediment was mixed into the water by hand until the sediment was completely liquefied. The gate was then opened and the debris-flow was released into the channel. The flow moved down the slope of the channel and spread out over the mouth slope. No internal turbulence was observable in the flow, and thus the flow was inferred to be in a laminar state. More detailed estimation of flow properties is in the discussion section.

The flow moved on the board for 9 s, and the velocity of the flow head was measured from digital video (Fig. 2) to decay exponentially from an initial velocity of about 1.47 m/s (Fig. 2) with a mean velocity of 0.09 m/s. A lobe of sediment 1.05 m long, 0.55 m wide, and an average of 2 cm thick was formed upon cessation of flow (Fig. 3). The lobe exhibited many surface wrinkles associated with flow movement

(Fig. 2), with wrinkles aligned transverse to the downcurrent direction in the central part of the lobe and arranged radially in marginal areas (Fig. 3). The lobe was dried until it became suitable for sampling (approximately 5 days). Deposits were sampled at points 5, 50, 70, and 100 cm from the mouth of the channel.

IMAGE ANALYSIS

Although digital image analysis for grain identification and measurement is not new (e.g., Russ 2002), recent advances in digital technology have led to remarkable progress in the sophistication of image analysis, and it is now possible to determine a range of grain properties such as size, shape, orientation, and spatial arrangement with a high degree of automation (Francus 1998). In the visualization method presented in this study, the grain-fabric is characterized by measuring the direction of grain elongation in images. Because grain analysis by the present method employs existing imaging techniques, it is described here only briefly for completeness. The analysis process involves sample preparation, image acquisition, image processing (preprocessing, classification, and postprocessing), and image analysis.

Sample Preparation and Image Acquisition

The unconsolidated samples were prepared as thin sections for microprobe observation. Sample surfaces were cemented using rapidly solidifying low-viscosity glue. The samples were then carefully removed from the channel or mouth slope, dried completely, and impregnated slowly and carefully with epoxy resin. The completely cemented samples were then split into specimens for measurement of grain imbrication (vertical flow, parallel section) and orientation (horizontal section).

Thin sections were observed and photographed by scanning electron microscopy

(SEM; JSM-6100, JEOL). Back-scattered electron (BSE) images were used for analysis. Due to the low atomic weight of the epoxy resin fixing the sediment matrix, the resin appeared distinctively darker than the clastic grains in the BSE images and the boundaries between the matrix and grains were clearly apparent. BSE images, which capture the profile of the top surface of the sample, are highly suitable for analysis of grain size and fabric (Francus 1998). SEM observations were made at a beam accelerating voltage of 25 keV, with a working distance of 34 mm. Images were obtained in 256-level grayscale from the SEM video output channel at a magnification of 50× and resolution of 1365 × 1024 pixels (594 pixels = 1 mm). The observations were repeated over the entire area of the sample, and a final mosaic image of the entire thin section was produced by joining images geometrically.

Image Processing

A binary image was produced from the 256-level grayscale BSE image mosaics (Fig. 4A), in which black pixels represent the epoxy resin matrix and white pixels represent clastic grains. The image-processing procedures involved preprocessing, classification, and postprocessing steps (described below), and all processing was performed on a computer using the public-domain ImageJ program (http://rsb.info.nih.gov/ij/) with custom software (http://www.kueps.kyoto-u.ac.jp/~naruse/english/java/) written in Java.

Preprocessing and Classification.--As a preprocessing step, image filtering (median filter) was applied to the acquired mosaic images to reduce random electronic noise introduced during BSE image acquisition. Image classification was then performed by dividing the image into regions corresponding to grain sections and the matrix using the *k*-means clustering classification scheme (Jain and Dubes 1998),

which is a brightness-based pixel classification procedure. Due to the good contrast between the resin-saturated matrix and quartz grains, the brightness histogram of the images exhibited clear peaks (Fig. 5), allowing the threshold brightness to be determined automatically. The classified mosaics were then converted to binary images (Fig. 4B).

Postprocessing.--Touching grains in the classified binary images were split by postprocessing. Grain contact, resulting mainly from overlapping projections of grains, noise, and limited image resolution, is a serious problem in automatic grain analysis, and several algorithms for separating touching grains have been proposed (e.g., van den Berg et al. 2002). This segmentation process is difficult, particularly for images acquired from thin sections with transmitted light. However, the opening process (Russ 2002) was found to be sufficient to separate merged grains in the BSE images obtained in the present study. The opening process combines erosion (removing grain pixels touching matrix pixels) followed by dilation (adding grain pixels adjacent to matrix pixels), and is effective for opening gaps between features that are just in contact. After automatic postprocessing, the images were checked visually and manual modifications applied where necessary to correct grain shapes.

Image Analysis

The location and elongation direction of grains were obtained as quantitative image-analysis data. The location was taken as the average of the x and y coordinates of all white pixels (grain pixels), and the elongation direction was obtained as the angle between the primary axis of an ellipse fitted to the grain by the Hough transform and the line parallel to the x axis of the image (Fig. 4C). All measured data are considered to be apparent two-dimensional characteristics of three-dimensional

features. The present study therefore examines only the apparent features of the debris-flow samples assuming equivalence to the three-dimensional structure. All analyses were performed automatically using the image analysis software ImageJ.

MAPPING OF GRAIN-FABRIC

The method for mapping of grain-fabric visualizes the "invisible" internal structure of massive sedimentary units as numerous small lines indicating the orientation of the grain-fabric (mean direction and vector concentration of grain elongation directions) in small local regions in the thin section. These lines are obtained automatically by image analysis, allowing a map of the grain-fabric of the entire deposit to be constructed.

The grain-fabric indicators are generated by statistical treatment of grain elongation directions in a circular sampling window (Fig. 4C). The mean direction $\bar{\theta}$ and the orientation strength R are calculated as follows:

$$\bar{\theta} = \arctan\left(\sum \sin\theta_i / \sum \cos\theta_i\right) \tag{1}$$

$$R = \sqrt{\left(\sum \sin\theta_i\right)^2 + \left(\sum \cos\theta_i\right)^2} \tag{2}$$

where θ_i is the measured elongation direction. The Watson-Stephens U^* test (Watson 1961; Stephens 1970) is applied to this subset of data, and, if the test is passed, the obtained directional is accepted as the preferred orientation. The 95% confidence interval of the mean direction is then calculated using the equation of Fisher and Lewis (1983):

$$\bar{\theta} \pm \arccos\left(1 - \frac{U_1(5)}{2\kappa R}\right) \tag{3}$$

where $U_1(5)$ is the upper 5% point of a χ_1^2 distribution and κ is the concentration parameter of the von Mises distribution estimated from the measured data set (Upton

and Fingleton 1989). After calculation of statistic values, the map is constructed. One line is drawn in the center of each sampling window if the data exhibit a statistically significant preferred orientation, with the orientation of the line representing the mean direction and length representing the vector concentration (Fig. 4C). The sampling window is then moved slightly, and the statistical treatment and line drawing is repeated. By this process, a map of the grain-fabric of the section is constructed (Fig. 4D). The calculation and display of the map are performed using the Java application (http://www.kueps.kyoto-u.ac.jp/~naruse/english/java/).

The grain-fabric map visualizes the internal variation of grain orientations in the sample. However, the appearance of the map is influenced by the interval between fabric lines and the radius of the sampling window, the latter of which determines the sample size and confidence interval of the mean direction. Because a smaller window provides a higher resolution of fabric information but incurs a larger statistical error (Fig. 6), the window diameter should be determined depending on the purpose of the study. In present paper, the radius of the sampling window was set to 1 mm, which is considered to provide sufficient resolution for the analysis of sedimentary structures while achieving a sufficiently narrow confidence interval (6–16°) for the mean orientation direction.

RESULTS

The four thin sections extracted from the debris-flow deposit at points 5, 50, 70 and 100 cm from the mouth of the channel were subjected to the grain-fabric analysis described above. All sampling points were located on the longitudinal center line of the depositional lobe, representing the downcurrent structural variation of the debris-flow deposit. None of the thin sections exhibited grading, lamination, or any other

visible sedimentary structures in macroscopic observation (Fig. 3). Image analysis indicates a mean grain size of 3.3phi, with only weak vertical and downcurrent grain-size segregation (Figs. 7, 8). Generally, most of samples, except for Sample 4 , show flow-parallel grain orientation, and all samples display upcurrent imbrication fabric (Fig. 9). However, the grain-fabric mapping of sample vertical sections reveals differences between samples collected from different downcurrent locations in the debris-flow deposit, as described in detail below.

Sample 1 (5 cm)

Sample Description.--This sample was obtained at the most upcurrent position (Fig. 3), where the flow condition changes most remarkably from flume flow (30º) to open shallow-slope flow (10º). The sample exhibits surficial wrinkle-like structures with a wavelength of 2–10 mm.

Fabric Map.--Three to four distinct lineation structures can be observed in the fabric map, from the lower left (upcurrent) to the upper right (downcurrent) (Fig. 10B), with grains oriented parallel to the lineation structures. The intervals between lineations consist of grains oriented almost vertical to the bedding plane. The distance between lineation structures varies from 0.5 to 3 mm.

Sample 2 (50 cm)

Sample Description.--This sample was obtained 50 cm from the mouth of the channel and almost corresponds to the longitudinal center of the depositional lobe (Fig. 3). The sample surface is almost entirely smooth but exhibits some trace wrinkle structures oriented transverse to the flow direction.

Fabric Map.--As a whole, grains in the section exhibit an obvious imbrication

(Fig. 11B). The imbrication angle tends to steepen upward, and the section can be divided vertically into three parts based on the mode of imbrication. In the lowermost part (0–3 mm), grains imbricate with a gentle angle (0–30°) that tends to steepen upward. In the intermediate part (3–14 mm), grains are uniformly imbricated with a steep angle (about 45°). In the uppermost part (14–18 mm), the grains form various fabric patterns, with most imbricated with steep angles (45–90°) but with some regions exhibiting no preferred imbrication (not statistically significant). These three horizons are separated by gradual transitions.

Sample 3 (70 cm)

Sample Description.--This sample was taken 70 cm from the channel mouth, just downcurrent of the center of the depositional lobe (Fig. 3). The sample surface is almost entirely smooth, but displays some trace wrinkle structures oriented transverse to the flow direction.

Fabric map.--Grains in the sample section are generally imbricated, with the imbrication varying somewhat (Fig. 12B). The section is composed of two indistinct horizons, each approximately 8 mm in thickness, characterized by a steepening-upward tendency of the grain imbrication angle. In the uppermost part of this sample, grains are randomly oriented and no grain-fabric can be identified.

Sample 4 (100 cm)

Sample Description.--This sample was extracted from the head of the depositional lobe, 100 cm from the channel mouth (Fig. 3). The sample surface exhibits wavy structures aligned transverse to the flow direction with a wavelength of 1–5 mm. The thickness of the sample is gradually thins downcurrent and terminates at

the distal end.

Fabric Map.--Although grains generally display gentle upcurrent imbrication (about 10°), an internal wavy structure formed by a variation in grain imbrication direction can be observed with a longitudinal transition from upcurrent to downcurrent imbrication (Fig. 13b). The wavelength of this internal structure ranges from 1 to 5 mm, roughly corresponding to the wavelength of the surface wrinkles.

DISCUSSION

General Sedimentological Characteristics of Debris-Flow Deposits

The debris-flow deposit reproduced in this study resembles recent and ancient debris-flow deposits in terms of several sedimentological characteristics. Recent debris-flow deposits are commonly observable in alluvial-fan and submarine-slope environments, and are characterized by a lobe-like geometry and surficial wrinkle structures interpreted as pressure ridges (Prior et al. 1984). Debris-flow deposits are also common in ancient strata deposited in both subaerial and submarine environments, and are characterized by poorly sorted massive structures (Mulder and Alexander 2001). Synsedimentary faults are occasionally observed in ancient debris-flow deposits (Massari 1984). The lobe-like geometry, surface wrinkles and massive structure are well reproduced by the experimental in this study.

The grain-fabric of the present laboratory samples is also analogous to those of natural debris-flow deposits. Several studies on the grain-fabric of debris-flow deposits (Taira and Scholle 1979; Taira 1989; Major 1998) have shown that grains are not randomly oriented, as commonly believed, but display a well-organized fabric characterized by flow-parallel or flow-transverse grain orientation and upcurrent imbrication (Hailwood and Ding 2000). Although traction sedimentation also

produces this type of grain-fabric (Allen 1984), debris-flow deposits typically exhibit high-angle grain imbrication (Taira 1989) or nearly horizontal imbrication (Enos 1977). High-angle upcurrent imbrication and flow-parallel grain orientation were produced in the present experiment (Fig. 9), resembling those of natural and previous experimental debris-flow deposits (Taira and Scholle 1979; Taira 1989).

The similar appearance of the experimental deposit and natural deposits does not mean that the experimental debris-flow is a complete natural analogue of debris-flows. The debris-flow deposit examined in this study lacks a significant cohesive mud fraction, and such noncohesive-debris-flows have various properties different from those of cohesive-debris-flows. For example, they are different in their rheological properties. Takahashi (1978) suggested that inertial debris-flows can be approximated as a dilatant fluid, although cohesive-debris-flows are Bingham fluids (Johnson, 1970). Besides, the experimental flow started at an unnaturally steep (30°) slope, it was not subaqueous, and it could not erode the substrate. Therefore, some processes different from those of natural debris-flows must have been work in the experimental flow.

However, estimation of the dimensionless numbers for the experimental flow suggests that the flow was a rough analogue of natural debris-flows in which grain friction stress and fluid viscosity are important as processes producting shear stress. Iverson (1997) reviewed the dimensional analysis of debris-flows based on several dimensionless numbers, such as:

$$N_{Sav} = \frac{\gamma^2 \rho_s d}{N(\rho_s - \rho_f) g \tan\phi} \tag{4}$$

$$N_{Bag} = \frac{v_s \gamma \rho_s d^2}{(1 - v_s)\mu} \tag{5}$$

$$N_{Dar} = \frac{\mu}{v_s \rho_s \gamma k} \tag{6}$$

where N is the number of grains above and including the layer of interest, γ is shear strain rate, ρ_s is mass density of the solid constituents of the debris-flow, ρ_f is mass density of the fluid constituents of the debris-flow, d is characteristic grain diameter, v_s is volume fraction of granular solids, μ is dynamic viscosity of the pore fluid, and k is hydraulic permeability. Estimating N, γ, ρ_s, ρ_f, d, v_s, μ and k are roughly 200, 10 (1/s), 2700 (kg/m^3), 1100 (kg/m^3), 1×10^{-4} (m), 0.5, 1×10^{-3} (Pas) and 1×10^{-11} (m^2), respectively, the Savage number N_{Sav} is 1×10^{-5}, which is below the criterion 0.1 and thus suggests that grain-friction stresses dominate grain-collision stress. Also, the Bagnold number N_{Bag} is 0.3, suggesting that viscous stresses dominate grain-collision stresses. The Darcy number N_{Dar} is 7×10^3, so that solid-fluid interactions may not be strong. Natural debris-flows (the Oddstad Debris-flow, South Toutle River, and the Osceola Mudflow) examined by Iverson (1997) all show similar characteristics; that is, the low Savage number (less than 2×10^{-4}), low Bagnold number (less than 4), and the high Darcy number (more than 6×10^4). Besides, a laminar state and instantaneous deposition are common to the experimental and natural flows. Such similarities may have reproduced some natural analogue processes in the experimental flow.

Sedimentary Structure from Grain-Fabric Maps

The grain-fabric mapping method employed in this study revealed a range of internal sedimentary structures in samples from the experimental debris-flow deposit, the most distinctive of which is that the grain-fabric of the debris-flow deposit varies remarkably through the lobe, even within the same thin section. Sample 2, which exhibited the simplest fabric structure of all the present samples, displayed a

steepening-upward tendency of grain imbrication angle (Fig. 11B), where grains are oriented nearly parallel to the bedding plane at the base of the section (where the vertical velocity gradient during the debris-flow would have been highest), and imbricated with a high upcurrent angle (about 45º) in the middle and upper horizons. At the most proximal end of the lobe (Sample 1), most grains are oriented vertically, but several lineation structures composed of upcurrent-inclined grains are also present (Fig. 10B). These lineation structures can be interpreted as synsedimentary thrusts, which are readily observable in many natural debris-flow deposits (e.g., Massari 1984). The identification of such thrust-like structures, which are invisible to the naked eye, demonstrates the effectiveness of grain-fabric mapping as a tool for analyzing granular materials such as sedimentary rocks.

A local variability of grain imbrication angle is also seen in other samples, suggesting that this type of variation may be a common feature of debris-flow deposits. The oscillation of grain imbrication angle in Samples 3 and 4 (Figs. 12, 13) may indicate the existence of internal flow structures (i.e., surges), which are often reported for natural and experimental debris-flow deposits (Major 1997; Mohrig et al. 1998), although the complexity of the structures makes interpretation difficult. It can be tentatively suggested that the faint horizontal layering seen in the fabric map of Sample 3 indicates surge boundaries, and the wavy structures in Sample 4 might represent the traces of surges climbing over previous surge deposits at the head of the flow, although it was impossible to observe internal structure of the moving flow directly.

In general terms, grains in regions with high velocity gradient during flow are oriented parallel to the shear plane (Fig. 14), whereas grains in regions of low velocity gradient tend to be imbricated with a relatively high angle or to be randomly oriented.

Mechanism of Formation of Preferred Grain-Fabric in Debris-Flows

Formation of grain-fabric in debris-flows can be expected to occur by a combination of several mechanisms. Although grain friction and fluid viscosity are significant in the experimental debris-flow with regard to flow shear stress, it is almost impossible to estimate quantitatively which processes are dominant for formation of grain-fabric because few previous experimental or theoretical data are available for such kind of analysis. Indeed, the experimental debris-flow analyzed in the present paper exhibits a heterogeneous grain-fabric with a range of sedimentary structures, even though it should exhibit primarily characteristics of a frictional-debris-flow. It therefore appears that the presence of such a range of structures in the grain-fabric map reflects the internal heterogeneity of flow properties.

Qualititatively, two simplified theoretical models have been proposed to explain the formation of preferred grain-fabric in debris-flow deposits: a grain-grain interaction model (Rees 1968) and a grain rotation model (Lindsay 1968). However, it should be noted that it is difficult to predict the behavior of granular materials in fluids precisely because of the large number of factors involved, including fluid movement, grain-fluid interaction, grain collision, and grain friction (Middleton and Hampton 1976; Lowe 1982; Mulder and Alexander 2001).

In the grain-grain interaction model proposed by Rees (1968), formation of grain-fabric in the debris flow (grain flow) is governed by grain collision. Generally, grains included in high-density granular flow are sufficiently close to collide frequently, resulting in frequent transfers of angular momentum between particles. This transfer of angular momentum between colliding grains is minimized when the long axes of the ellipsoidal grains are aligned perpendicular to the collision axis, such

that grains in adequately sustained flow acquire a preferred imbrication that is oriented perpendicular to the mean collision axis of grains. Because grains in the upper region of laminar flow are transported faster than those in the lower region, grains tend to collide with grains lower in the flow, resulting in the orientation of the mean collision axis in an upcurrent-upper direction. According to the experimental results of Bagnold (1954), the mean collision axis in sheared grain flow is inclined 30–40° upcurrent (Taira 1989), irrespective of the flow shear rate or position in the flow. As a result, grains in debris-flow are theoretically expected to show relatively high-angle (30–40°) upcurrent imbrication. Indeed, Taira (1989) reported that experimental debris-flow deposits exhibit higher imbrication angles (15–35°) than traction sedimentation deposits (10–20°). This high upcurrent imbrication angle (~ 45°) was also observed in the middle and upper horizons of Sample 2 in the present study, supporting the grain-grain interaction model.

However, it is also known that grains in laminar flow can acquire preferred orientation without grain collision. Lindsay (1968) calculated the rotation of ellipsoidal grains in laminar flow using the theory of Jeffery (1922) in an analysis of the grain-fabric of cohesive-debris-flow deposits. In this case, grains rotate vertically due to the vertical velocity gradient of laminar flow, and the rotation velocity is minimum when the long axes are oriented parallel to the flow direction. Therefore, the long axes of grains in adequately sustained flow tend to become oriented parallel to flow with slight oscillations. Such flow-parallel orientation fabrics have been reported for several cohesive-debris-flow deposits (Lindsay 1968; Enos 1977), and the fabric maps in the present paper also show that grains in the lower horizon of Sample 2 are oriented parallel to the flow direction, whereas grains included in the synsedimentary thrusts of Sample 1 are oriented parallel to the inferred shear planes.

In both situations, the velocity gradient of the fluid and the particle density are inferred to be very high. The grain-rotation effect may be dominant in basal layer of the flow rather than the grain-collision effect, because the high particle concentration is considered to induce nearly continuous grain contact and therefore hinder grain collision (Iverson, 1997; Takahashi 2001). However, both grain collision and rotation can be expected to occur in natural debris-flow, and the properties of the debris-flow may therefore vary locally even in single-layered flow because of variations in the particle density and the velocity gradient.

Other mechanisms may also work to form grain imbrication. Some part of the samples examined in present paper show extremely higher angles of imbrication than in the studies that Taira (1989) reviewed. The high angle of imbrication (> 35°) may result from vertical fluid escape, because the experimental flow lacks a mud fraction and the fluid escape may play an essential role as a grain-supporting mechanism in such flows (Middleton and Hampton 1976). Future investigations seem necessary to estimate more accurate causes of development of grain imbrication.

Massive Structure in Sediment-Gravity-Flow Deposits

The various interpretations of massive deposits tend to be in direct opposition. At high rates of sediment supply (> 0.67 mm/s), which can be correlated with sustained high-density turbidity currents, bedform formation is hindered, resulting in the formation of a massive deposit (Arnott and Hand 1989). However, instantaneous deposition, as in debris-flow, is also know to form massive deposits (Shanmugam 1996). From the viewpoint of the depositional process, the massive structure of the deposits of high-density turbidity currents is therefore quite different from that of debris-flow, although the final deposits appear essentially identical upon visual

inspection (Sohn 1997). The primary difference between the two processes is that the internal structure of the original flow may be preserved in debris-flow deposits as a result of instantaneous deposition. In contrast, turbidites can preserve the information only of the basal part of the flow because of the continuous grain-by-grain accumulation of sediment (Kneller and Branney 1995). The use of grain-fabric maps proved useful in the present study for revealing the crypt structure of the massive division of debris-flow deposits (Figs. 10-13), which appear on a macroscopic scale to be identical. The sedimentary structures described by the grain-fabric, such as synsedimentary thrusts, appear to reflect the internal structures of flow during deposition, although accurate interpretation remains difficult.

The method of grain-fabric mapping allows structural features not discernible by conventional analyses of grain size to be visualized. Thus, grain-fabric mapping can reveal traces of sedimentary process that do not induce grain-size sorting, which is the case for massive sedimentation structures (e.g., “freezing” deposition of debris-flow). Fabric mapping should be effective for analyzing massive deposits and interpreting the depositional processes. The method should be applied to other experimental and natural deposits in order to confirm that the results obtained here are general features of debris-flow deposits. The application of this method to the deposits of high-density turbidity currents and other massive deposits is also expected to reveal interesting results.

CONCLUSIONS

Grain-fabric mapping was presented and applied to analysis of the internal structure of an experimental massive debris-flow deposit. The debris-flow deposit was produced using a 30° inclined flume expanding onto a 10° slope. Transverse thin

sections were prepared from the depositional lobe at four longitudinal points and imaged by SEM. Grain-fabric mapping was then performed automatically using the processed back-scattered electron images. Although the massive sedimentary samples appeared structureless by macroscopic observation, the grain-fabric map revealed various sedimentary structures, including distinct lineations from lower-upcurrent to upper-downcurrent in the most proximal sample (interpreted as synsedimentary thrusts), a steepening-upward trend of grain imbrication angle in intermediate samples with very low-angle imbrication in the basal horizon indicative of high shear rate flow, and complex imbrication features in the most distal samples. Thus, the technique for grain-fabric mapping presented in this study has the ability to visualize a range of sedimentary structures that are not observable with the naked eye or by analyses of grain size or color. As such, grain-fabric mapping appears to be particularly useful for the analysis of massive deposits. The method proved to be effective for the investigation of experimental debris-flow deposits in the present study.

ACKNOWLEDGMENTS

This manuscript benefited from thoughtful reviews by Jaco Baas and Ernie Hailwood. We would like to thank Editor Colin North and Associate Editor Peter Talling. Gratitude is extended to the staff and researchers of the Department of Geology & Mineralogy, Kyoto University, and in particular to Dr. H. Maeda for guidance throughout this study. Dr. T. Sakai and M. Yokokawa are also gratefully acknowledged for helpful discussion and advice. This research was supported in part by a Grant-in-Aid for Young Scientists (B) (16740287, 2004) from the Ministry of Education, Science, Sports, Culture and Technology of Japan.

REFERENCES

Allen, J.R.L., 1984, Sedimentary Structures, Vol. 1: Amsterdam, Elsevier Publishing Company, 593 p.

Allen, J.R.L., 1991, The Bouma division A and the possible duration of turbidity currents: Journal of Sedimentary Petrology, v. 61, p. 291-295.

Arnott, R.W.C., and Hand, B.M., 1989, Bedforms, primary structures and grain-fabric in the presence of suspended sediment rain: Journal of Sedimentary Petrology, v. 59, p. 1062-1069.

Bagnold, R.A., 1954, Experiments on a gravity-free dispersion of large solid sheres in a Newtonian fluid under shear: Royal Society (London), Proceedings, Series A, Mathematical and Physical Sciences, v. 225, p. 49-63.

Bouma, A.H., 1962, Sedimentology of Some Flysch Deposits; a Graphic Approach to Facies Interpretation: Amsterdam, Elsevier Publishing Company, 168 p.

Enos, P., 1977, Flow regimes in debris flow: Sedimentology, v. 24, p. 133-142.

Fisher, N.I., and Lewis, T., 1983, Estimating the common mean direction of several circular or spherical distributions with differing dispersions: Biometrika, v. 70, p. 333-341.

Francus, P., 1998, An image-analysis technique to measure grain-size variation in thin sections of soft clastic sediments: Sedimentary Geology, v. 121, p. 289-298.

Hailwood, E.A., and Ding, F., 2000, Sediment transport and dispersal pathways in the Lower Cretaceous sands of the Britannia Field, derived from magnetic anisotropy: Petroleum Geoscience, v. 6, p. 369-379.

Iverson R.M., 1997, The physics of debris flows: Reviews of Geophysics, v. 35, p. 245-296.

Jain, A.K. and Dubes, R.C. 1988, Algorithms for Clustering Data: New Jersey, Prentice Hall, 334 p.

Jeffery, G.B., 1922, The motion of ellipsoidal particles immersed in a viscous fluid: Royal Society (London), Proceedings, Series A, Mathematical and Physical Sciences, v. 102, p. 161-179.

Johnson, A.M., 1970, Physical Processes in Geology: San Francisco, Freeman, 571 p.

Kneller, B.C., and Branney, M.J., 1995, Sustained high-density turbidity currents and the deposition of thick massive sands: Sedimentology, v. 42, p. 607-616.

Lindsay, J.F., 1968, The development of clast fabric in mudflows: Journal of Sedimentary Petrology, v. 38, p. 1242-1253.

Lowe, D.R., 1982, Sediment gravity flows; II, Depositional models with special reference to the deposits of high-density turbidity currents: Journal of Sedimentary Petrology, v. 52, p. 279-297.

Lowe, D.R., 1988, Suspended-load fallout rate as an independent variable in the analysis of current structures: Sedimentology, v. 35, p. 765-776.

Major, J.J., 1997, Depositional processes in large-scale debris-flow experiments: Journal of Geology, v. 105, p. 345-366.

Major, J.J., 1998, Pebble orientation on large, experimental debris-flow deposits: Sedimentary Geology, v. 117, p. 151-164.

Massari, F., 1984, Resedimented conglomerates of a Miocene fan-delta complex, Southern Alps, Italy, *in* Koster E.H. and Steel R.J., eds., Sedimentology of Gravels and Conglomerates, Memoir - Canadian Society of Petroleum Geologists 10: Calgary, Canadian Society of Petroleum Geologists, p. 259-278.

Middleton, G.V. and Hampton, M.A., 1976, Subaqueous sediment transport and

deposition by sediment gravity flows, *in* Stanley, D.J., and Swift, D.J.P., eds., Marine Sediment Transport and Environmental Management: New York, John Wiley & Sons, p. 197-218.

Mohrig, D., Whipple, K.X., Hondzo, M., Ellis, C., and Parker, G., 1998, Hydroplaning of subaqueous debris flows: Geological Society of America, Bulletin, v. 110, p. 387-394.

Mulder, T., and Alexander, J., 2001, The physical character of subaqueous sedimentary density flows and their deposits: Sedimentology, v. 48, p. 269-299.

Postma, G., 1986, Classification for sediment gravity-flow deposits based on flow conditions during sedimentation: Geology, v. 14, p. 291-294.

Prior, D.B., Bornhold, B.D., and Johns, M.W., 1984, Depositional characteristics of a submarine debris flow: Journal of Geology, v. 92, p. 707-727.

Rees, A.I., 1968, The production of preferred orientation in a concentrated dispersion of elongated and flattened grains: Journal of Geology, v. 76, p. 457-465.

Russ, J.C. 2002, The Image Processing Handbook, Fourth Edition: Boca Ration, Florida, CRC Press, 732 p.

Shanmugam, G., 1996, High-density turbidity currents; are they sandy debris flows?: Journal of Sedimentary Research, v. 66, p. 2-10.

Shanmugam, G., 2000, 50 years of the turbidite paradigm (1950s-1990s); deep-water processes and facies models; a critical perspective, *in* Stow, D.A.V., and Mayall, M., eds., Deep-Water Sedimentary Systems; New Models for the 21st Century: Oxford, U.K., Pergamon, p. 285-342.

Slatt, R.M., Weimer, P., Stone, C.G., Lowe, D.R., Coleman Jr, J.L., Bouma, A.H., DeVries, M.B., Stone, C.G., D'Agostino, A.E., Jordan, D.W., Shanmugam,

G., and Moiola, R.J., 1997, Reinterpretation of depositional processes in a classic flysch sequence (Pennsylvanian Jackfork Group), Ouachita Mountains, Arkansas and Oklahoma; discussions and reply: American Association of Petroleum Geologists, Bulletin, v. 81, p. 449-491.

Sohn, Y.K., 1997, On traction-carpet sedimentation: Journal of Sedimentary Research, v. 67, p. 502-509.

Stephens, M.A., 1970, Use of the Kolmogorov-Smirnov, Cramer-von Mises and related statistics without extensive tables: Royal Statistical Society, Journal, Series B, v. 32, p. 115-122.

Stow, D.A.V., and Johansson, M., 2000, Deep-water massive sands: nature, origin and hydrocarbon implications, *in* Stow, D.A.V., and Mayall, M., eds., Deep-Water Sedimentary Systems; New Models for the 21st Century: Oxford, U.K., Pergamon, p. 145-174.

Taira, A., 1989, Magnetic fabrics and depositional processes, *in* Taira, A., and Masuda, F., eds., Sedimentary Facies in the Active Plate Margin: Tokyo, Terra Scientific Publication Co., p. 43-77.

Taira, A. and Scholle, P.A., 1979, Deposition of resedimented sandstone beds in the Pico Formation, Ventura Basin, California, as interpreted from magnetic fabric measurements: Geological Society of America, Bulletin, v. 90, p. I 952-I 962.

Takahashi, T., 1978, Mechanical characteristics of debris flow: American Society of Civil Engineers, Proceedings, Journal of the Hydraulics Division, v. 104, p. 1153-1169.

Takahashi, T., 2001, Mechanics and simulation of snow avalanches, pyroclastic flows and debris flows, *in* McCaffrey, W.D., Kneller, B.C., and Peakall, J.,

eds., Particulate Gravity Currents: Oxford, U.K., Blackwell, p. 11-43.

Upton, G.J.G., and Fingleton, B., 1989, Spatial Data Analysis by Example - Volume 2, Categorical and Directional Data: 2, New York, John Wiley & Sons, 416 p.

van den Berg, E.H., Bense, V.F., and Schlager, W., 2003, Assessing textural variation in laminated sands using digital image analysis of thin sections: Journal of Sedimentary Research, v. 73, p. 133-143.

van den Berg, E.H., Meesters, A.G.C.A., Kenter, J.A.M. and Schlager, W., 2002, Automated separation of touching grains in digital images of thin sections: Computers and Geosciences, v. 28, p. 179-190.

Watson, G.S., 1961, Goodness of fit tests on a circle, I: Biometrika, v. 48, p. 109-114.

Yagishita, K., 1994, Antidunes and traction-carpet deposits in deep-water channel sandstones, Cretaceous, British Columbia, Canada: Journal of Sedimentary Research, Section A, v. 64, p. 34-41.

Figure captions

Figure 1. Channel and board for simulation of debris-flow.

Figure 2. Head velocity of experimental debris-flow measured from digital video data.

Figure 3. Experimental debris-flow deposit with sampling points indicated by arrows.

Figure 4. Procedures for image analysis. (A) BSE image of sample in 256-level grayscale. (B) Binarized image produced by k-means clustering. (C) Sampling window and best-fit ellipses overlaid on the binary image. (D) Final grain-fabric map.

Figure 5. Histogram of distribution of gray values in the analyzed image (Sample 1), showing clear peaks assignable as grains and the resin matrix.

Figure 6. Scatter diagram plotting radius of sampling window against the number of sampled grains and the mean confidence intervals of the calculated vector mean

Figure 7. Downcurrent grain-size variation in experimental debris-flow deposit.

Figure 8. Vertical grain-size variation in experimental debris-flow deposit.

Figure 9. Rose diagrams showing the results of horizontal and vertical fabric measurement. Horizontal sections were cut parallel to the bedding plane, and vertical sections were cut along the longitudinal axis of the depositional lobe. All samples

display upcurrent imbrication fabric in their vertical sections, and samples 1-3 show flow-parallel grain orientation in their horizontal sections whereas no preferred orientation can be observed in the horizontal section of Sample 4.

Figure 10. (A) BSE image and (B) grain-fabric map of Sample 1. Detailed explanation is in the text.

Figure 11. (A) BSE image and (B) grain-fabric map of Sample 2. Detailed explanation is in the text.

Figure 12. (A) BSE image and (B) grain-fabric map of Sample 3. Detailed explanation is in the text.

Figure 13. (A) BSE image and (B) grain-fabric map of Sample 4. Detailed explanation is in the text.

Figure 14. Inferred internal structures of experimental debris-flow deposit.

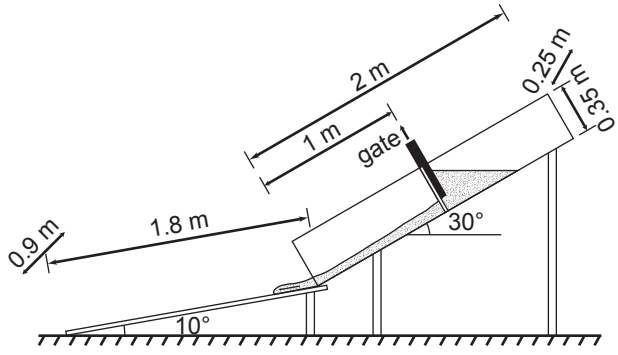

Figure 1. Naruse and Masuda

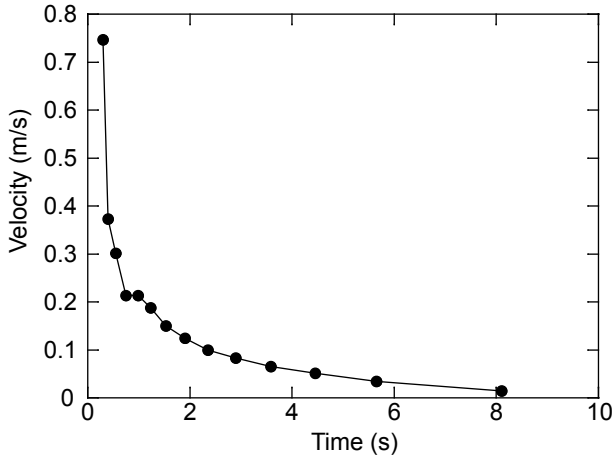

Figure 2. Naruse and Masuda

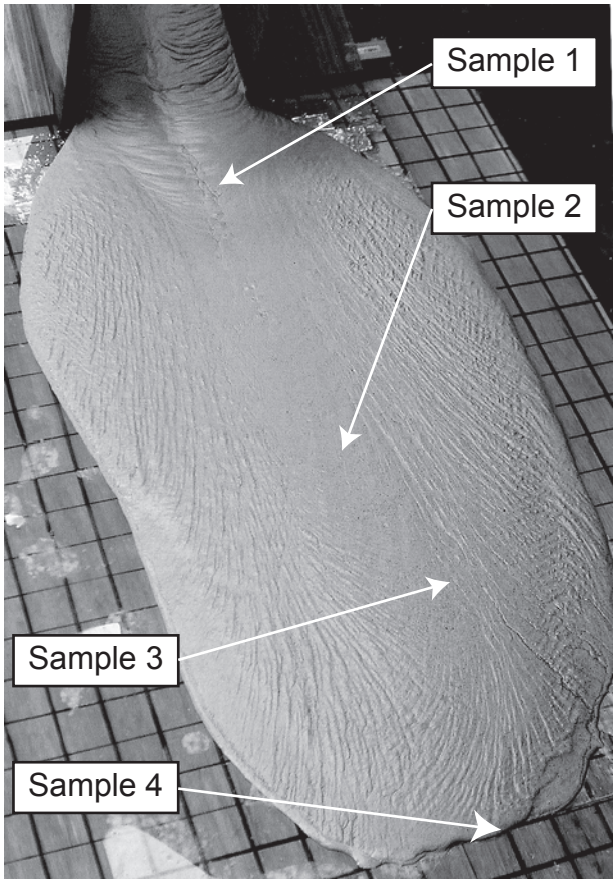

Figure 3. Naruse and Masuda

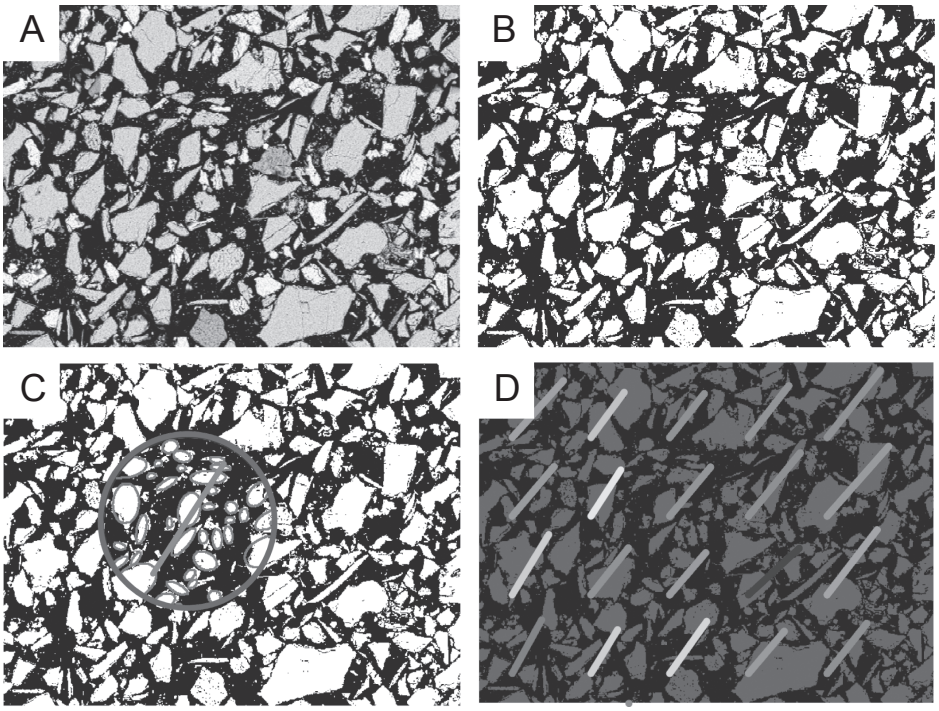

Figure 4. Naruse and Masuda

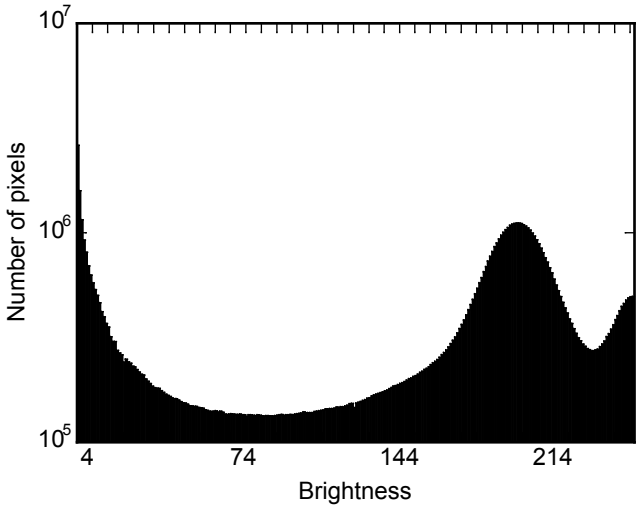

Figure 5. Naruse and Masuda

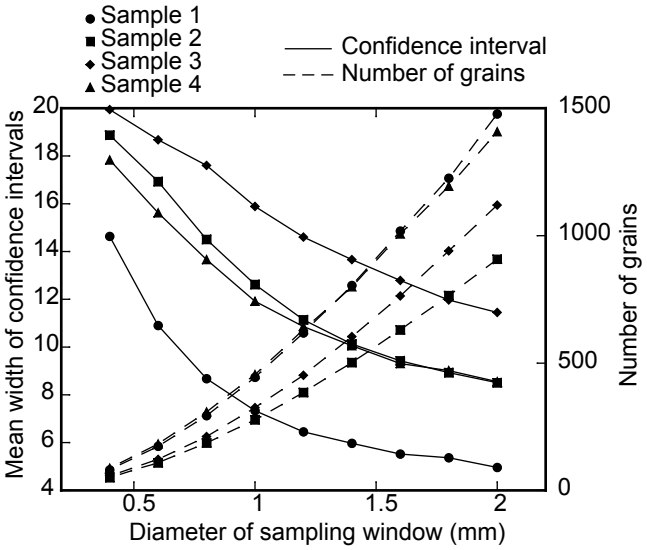

Figure 6. Naruse and Masuda

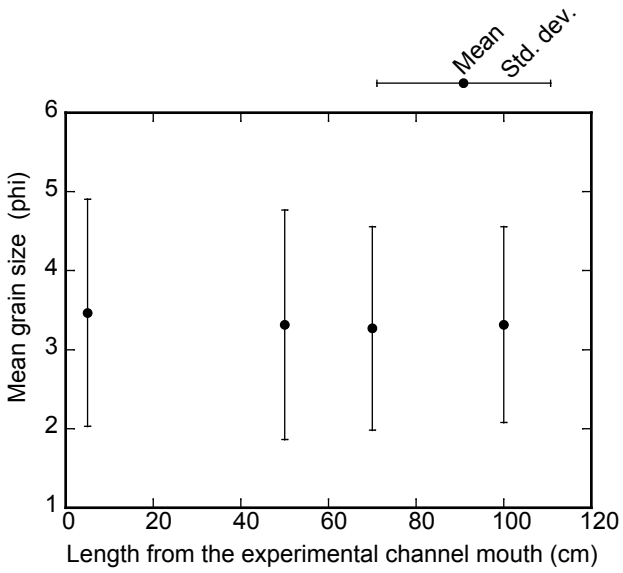

Figure 7. Naruse and Masuda

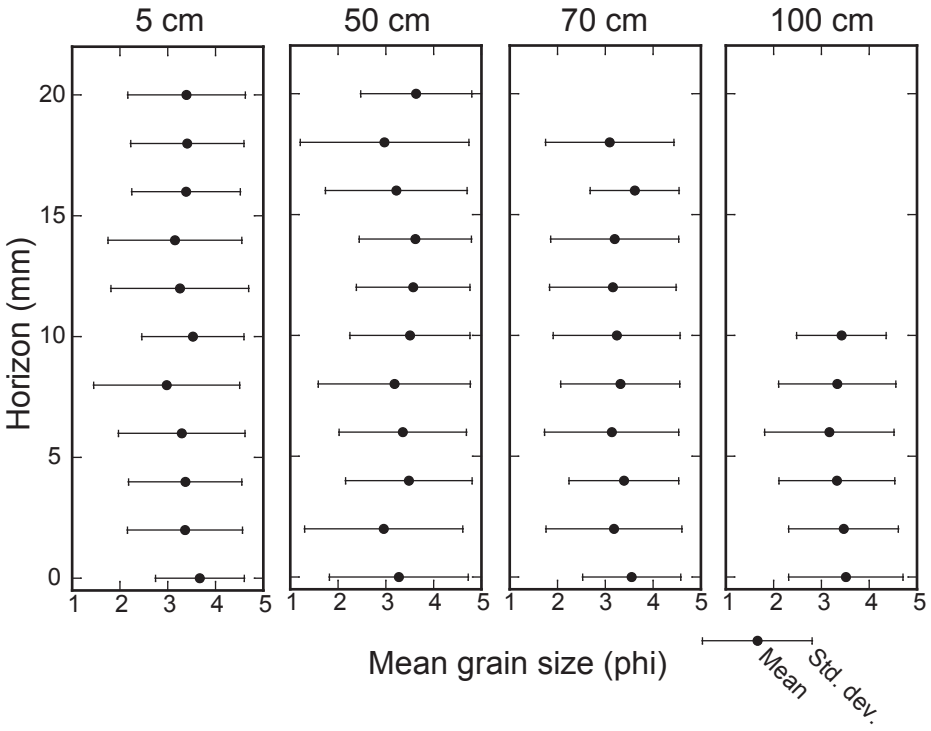

Figure 8. Naruse and Masuda

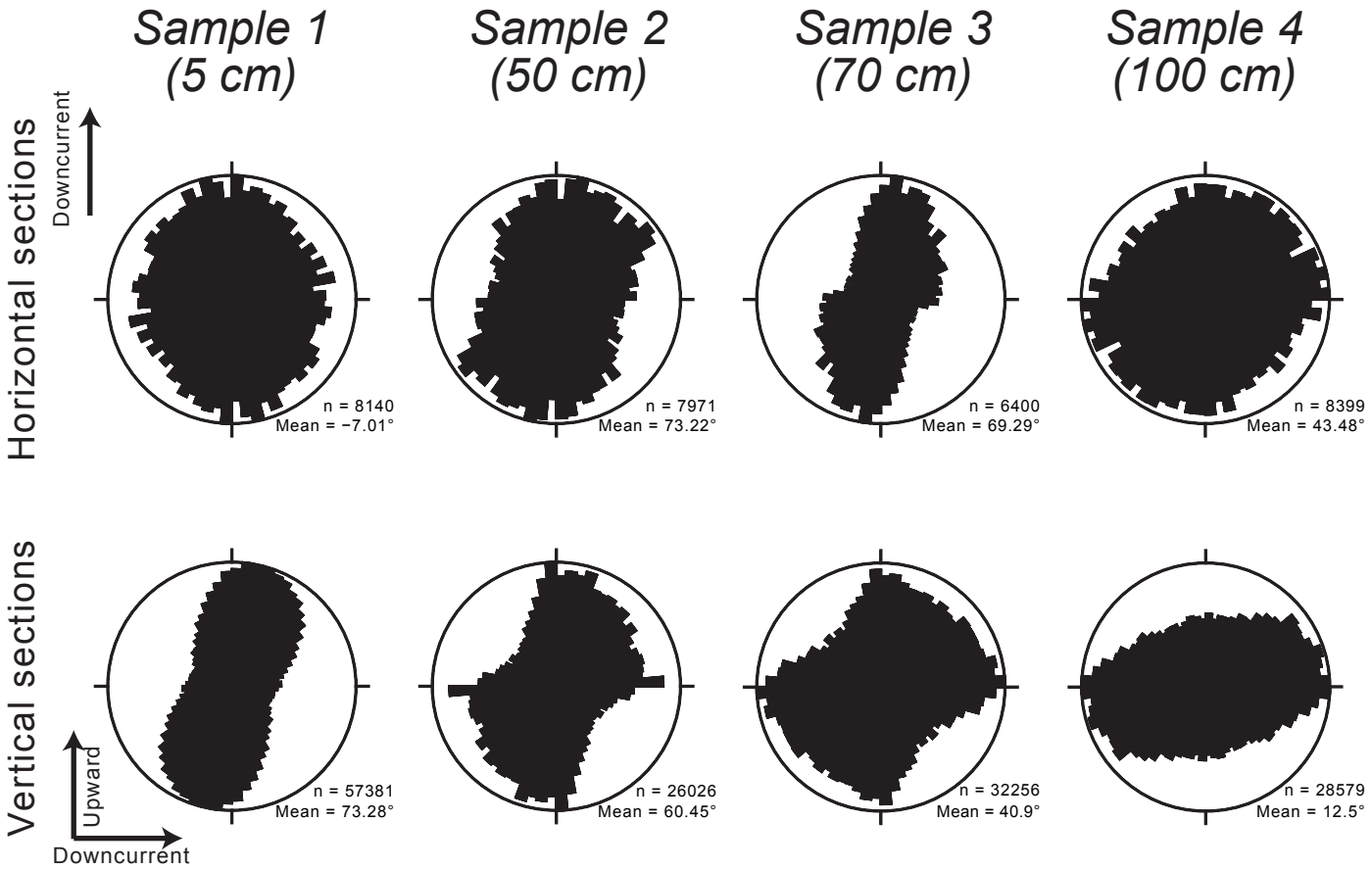

Figure 9. Naruse and Masuda

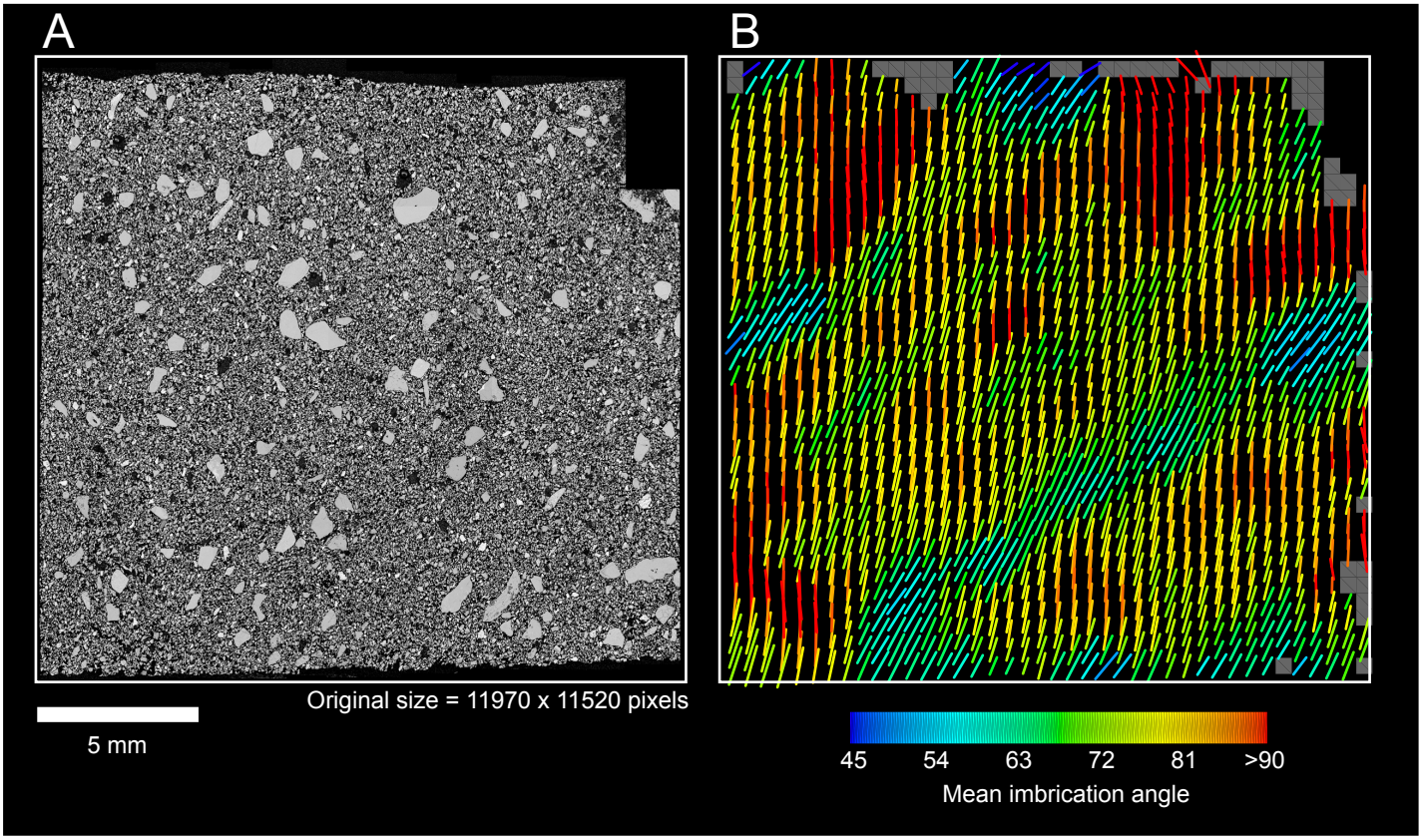

Figure 10. Naruse and Masuda

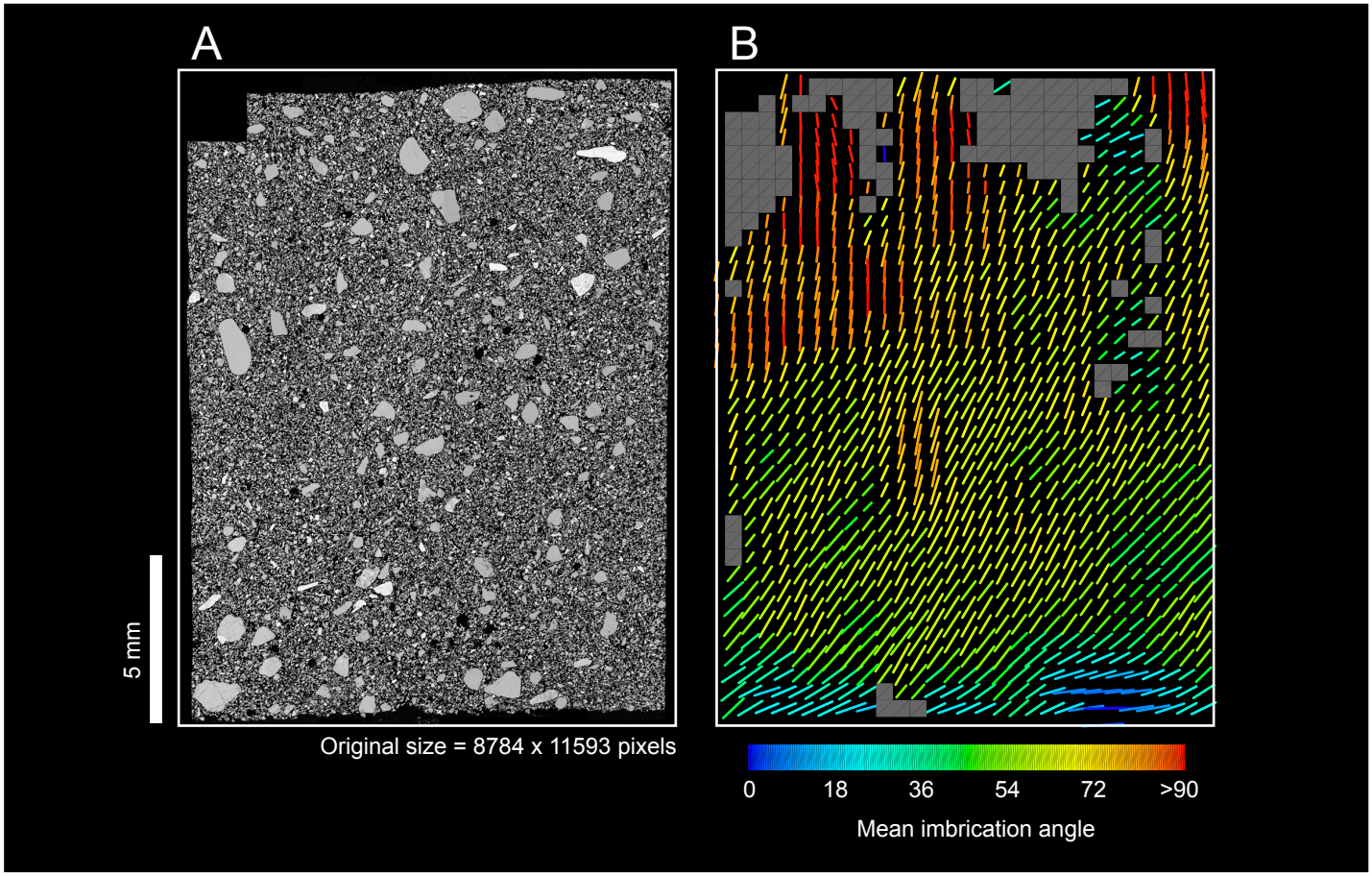

Figure 11. Naruse and Masuda

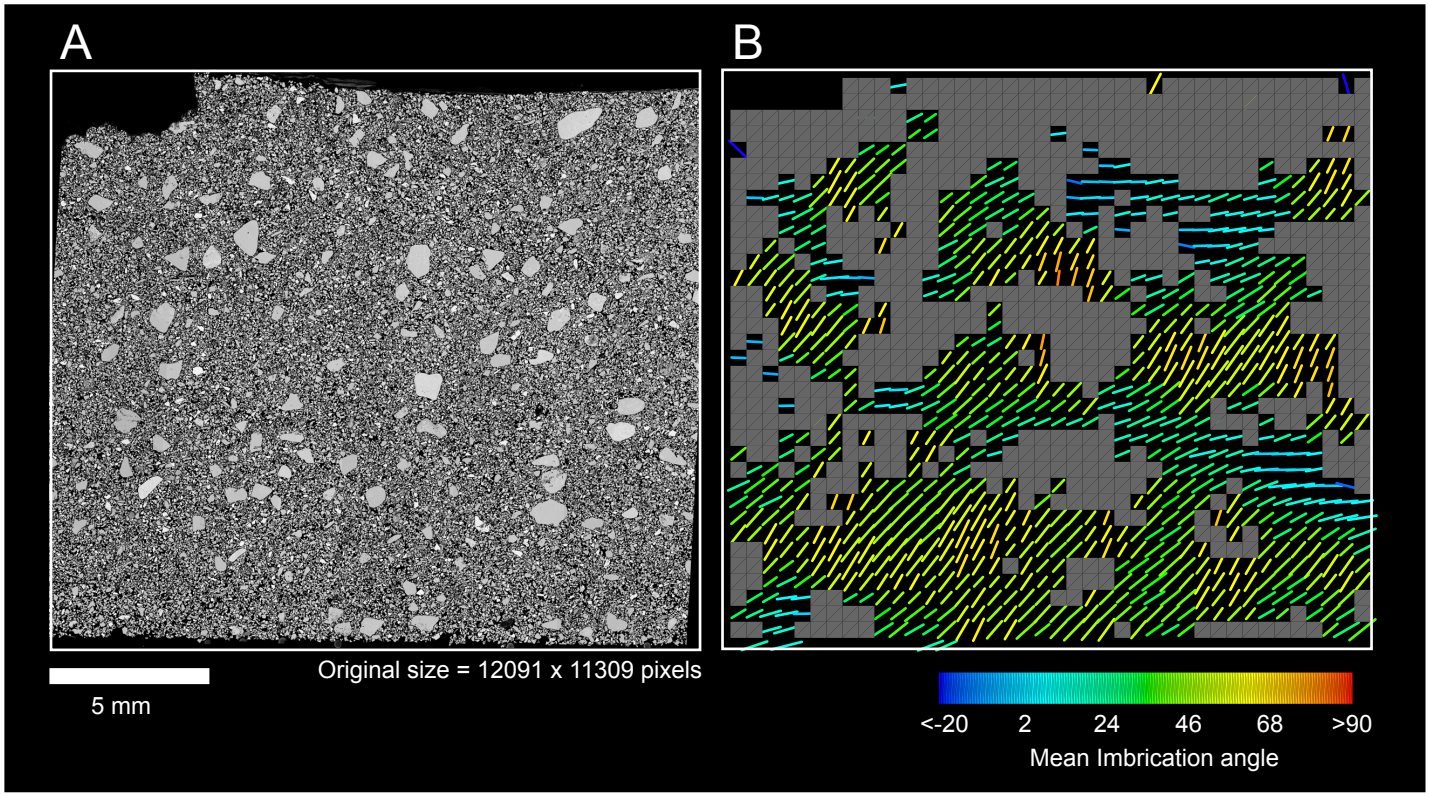

Figure 12. Naruse and Masuda

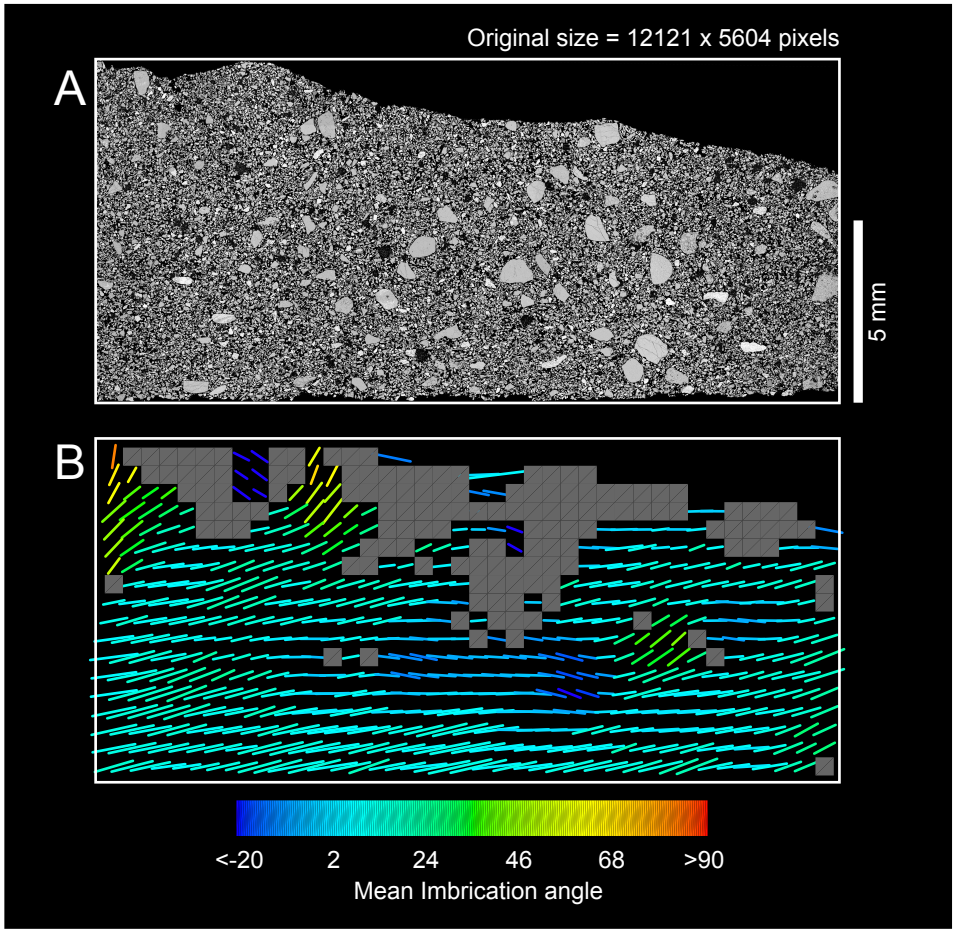

Figure 13. Naruse and Masuda

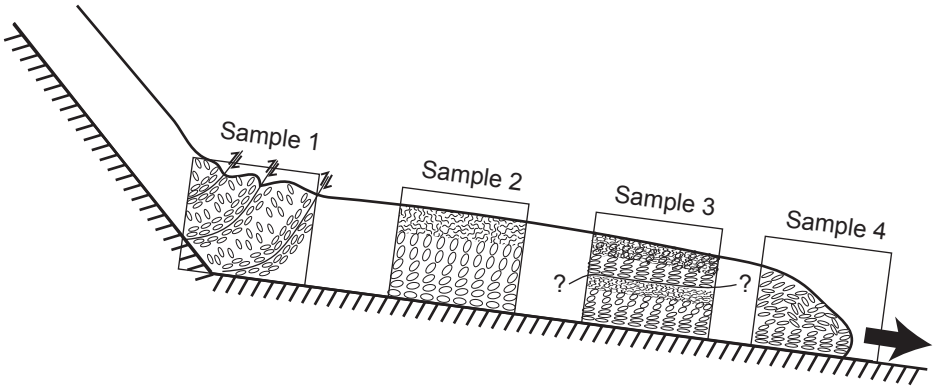

Figure 14. Naruse and Masuda